The ALMA-ALPINE [CII] survey: Kennicutt-Schmidt relation in four massive main-sequence galaxies at z ~ 4.5

Downloaded from: https://research.chalmers.se, 2025-12-04 23:28 UTC

Citation for the original published paper (version of record):
Béthermin, M., Accard, C., Guillaume, C. et al (2023). The ALMA-ALPINE [CII] survey: Kennicutt-Schmidt relation in four massive main-sequence galaxies at z ~ 4.5. Astronomy and Astrophysics, 680. http://dx.doi.org/10.1051/0004-6361/202348115

N.B. When citing this work, cite the original published paper.

research.chalmers.se offers the possibility of retrieving research publications produced at Chalmers University of Technology. It covers all kind of research output: articles, dissertations, conference papers, reports etc. since 2004. research.chalmers.se is administrated and maintained by Chalmers Library

(article starts on next page)

A&A 680, L8 (2023)
https://doi.org/10.1051/0004-6361/202348115
© The Authors 2023

Astronomy & Astrophysics

LETTER TO THE EDITOR

The ALMA-ALPINE [CII] survey: Kennicutt-Schmidt relation in four massive main-sequence galaxies at $z \sim 4.5$

M. Béthermin[1,2], C. Accard[1,⋆], C. Guillaume[1,⋆], M. Dessauges-Zavadsky[3], E. Ibar[4], P. Cassata[5,6], T. Devereaux[5,6], A. Faisst[7], J. Freundlich[1], G. C. Jones[8], K. Kraljic[1], H. Algera[9,10], R. O. Amorín[11,12], S. Bardelli[19], M. Boquien[13], V. Buat[2], E. Donghia[14], Y. Dubois[15], A. Ferrara[16], Y. Fudamoto[29], M. Ginolfi[30,31], P. Guillard[15], M. Giavalisco[17], C. Gruppioni[19], G. Gururajan[18,19], N. Hathi[20], C. C. Hayward[21], A. M. Koekemoer[20], B. C. Lemaux[22,33], G. E. Magdis[23,24,25], J. Molina[26], D. Narayanan[23,27], L. Mayer[32], F. Pozzi[19], F. Rizzo[23,25], M. Romano[6,28], L. Tasca[2], P. Theulé[2], D. Vergani[19], L. Vallini[19], G. Zamorani[19], A. Zanella[6], and E. Zucca[19]

(Affiliations can be found after the references)

Received 29 September 2023 / Accepted 13 November 2023

ABSTRACT

Aims. The Kennicutt-Schmidt (KS) relation between the gas and the star formation rate (SFR) surface density ($\Sigma_{\rm gas}-\Sigma_{\rm SFR}$) is essential to understand star formation processes in galaxies. To date, it has been measured up to $z \sim 2.5$ in main-sequence galaxies. In this Letter our aim is to put constraints at $z \sim 4.5$ using a sample of four massive main-sequence galaxies observed by ALMA at high resolution.

Methods. We obtained ∼0.3″-resolution [CII] and continuum maps of our objects, which we then converted into gas and obscured SFR surface density maps. In addition, we produced unobscured SFR surface density maps by convolving *Hubble* ancillary data in the rest-frame UV. We then derived the average $\Sigma_{\rm SFR}$ in various $\Sigma_{\rm gas}$ bins, and estimated the uncertainties using a Monte Carlo sampling.

Results. Our galaxy sample follows the KS relation measured in main-sequence galaxies at lower redshift, and is slightly lower than the predictions from simulations. Our data points probe the high end both in terms of $\Sigma_{\rm gas}$ and $\Sigma_{\rm SFR}$, and gas depletion timescales (285–843 Myr) remain similar to $z \sim 2$ objects. However, three of our objects are clearly morphologically disturbed, and we could have expected shorter gas depletion timescales ($\lesssim$100 Myr) similar to merger-driven starbursts at lower redshifts. This suggests that the mechanisms triggering starbursts at high redshift may be different than in the low- and intermediate-z Universe.

Key words. galaxies: high-redshift – galaxies: ISM – galaxies: star formation – submillimeter: galaxies

1. Introduction

The Kennicutt-Schmidt (KS) empirical relation (Schmidt 1963; Kennicutt 1998; de los Reyes & Kennicutt 2019) linking the gas and the star formation rate (SFR) surface densities ($\Sigma_{\rm gas} - \Sigma_{\rm SFR}$) is a key tool for understanding the star formation in galaxies across cosmic times. This relation has been vastly explored in the local Universe including at sub-galactic scales (e.g., Leroy et al. 2013; Pessa et al. 2021; Sun et al. 2023). These studies have also shown that star formation is mainly correlated with the molecular gas (e.g., Bigiel et al. 2008).

At higher redshift, these measurements are difficult, since they require resolved maps of the molecular gas, usually using the CO rotational lines, together with reliable star formation maps (e.g., Molina et al. 2019). Since current observing facilities are not sensitive enough to detect the atomic hydrogen at 21 cm in the high-redshift Universe, previous and current studies mainly focused on the molecular KS relation. In the rest of this Letter, we only discuss this molecular version. Measurements integrated at the full-galaxy scale up to $z \sim 2.5$ showed that most galaxies lie on the local KS relation, but at higher gas surface density (e.g., Tacconi et al. 2013; Freundlich et al. 2019). Most of these high-redshift galaxies also follow a SFR–stellar mass ($M_\star$) relation, also known as the main sequence of star-forming galaxies (e.g., Noeske et al. 2007; Elbaz et al. 2007). The normalization of this main sequence increases rapidly with increasing redshift (e.g., Schreiber et al. 2015) together with the gas fraction (e.g., Magdis et al. 2012; Saintonge et al. 2013; Béthermin et al. 2015), suggesting that the larger gas reservoirs are driving the higher specific SFR ($\rm sSFR = SFR/M_\star$) observed at high z.

However, a small population of starbursts with a $\Sigma_{\rm SFR}$ excess compared to the KS relation of main-sequence galaxies was found by Genzel et al. (2010) and Daddi et al. (2010), among others. Resolved studies of high-z starbursts confirmed the $\Sigma_{\rm SFR}$ excess at sub-galactic scale in these systems (e.g., Freundlich et al. 2013; Rawle et al. 2014; Hodge et al. 2015). Another population of starbursts with an SFR excess was also identified above the main sequence (e.g., Rodighiero et al. 2011). The starburst populations observed in both relations are suspected to be driven by mergers (e.g., Sargent et al. 2014; Cibinel et al. 2019).

To date, the KS relation in $z > 2.5$ main-sequence galaxies has remained unexplored. However, the Atacama Large Millimeter Array (ALMA) has opened new perspectives to explore earlier times. In particular, the bright 158 µm rest-fame [CII] line is now easily observable from the ground at $z \gtrsim 4$, and

⋆ The second and third authors are master's students, who had a similar contributions to this Letter (analysis of the first three sources and initial results).

Open Access article, published by EDP Sciences, under the terms of the Creative Commons Attribution License (https://creativecommons.org/licenses/by/4.0), which permits unrestricted use, distribution, and reproduction in any medium, provided the original work is properly cited.
This article is published in open access under the Subscribe to Open model. Subscribe to A&A to support open access publication.

can be used as a gas tracer (e.g., Zanella et al. 2018). Recently, Vallini et al. (2024) published a study on the KS relation in five $z \sim 7$ bright Lyman beak galaxies (LBGs), but the main-sequence nature of these galaxies remains unclear. The ALMA large program to investigate [CII] at early times (ALPINE, Le Fèvre et al. 2020; Béthermin et al. 2020; Faisst et al. 2020) built a sample of 118 main-sequence galaxies at $4 < z < 6$, observed in [CII] and continuum at low angular resolution (~1″, marginally or not resolved). In this sample, Dessauges-Zavadsky et al. (2020) found a flattening of the evolution of the gas fraction with redshift, similar to that observed for the sSFR (Khusanova et al. 2021). In contrast, Jones et al. (2021) and Romano et al. (2021) estimated that a high fraction (~40%) of these objects exhibits morpho-kinematical signatures of mergers despite being on the main sequence, suggesting that the mechanisms driving star formation in the $z \gtrsim 4$ Universe may differ from lower redshifts.

In this Letter we explore the KS relation at $z \sim 4.5$ using a sample of four ALPINE galaxies followed up at higher resolution (~0.3 arcsec, 2 kpc) by ALMA. In Sect. 2 we describe our observations and the data analysis. We then present our new results on the KS relation in Sect. 3. Finally, we discuss them and conclude in Sect. 4. We assume a flat ΛCDM cosmology ($h = 0.7$, $\Omega_\Lambda = 0.7$, $\Omega_m = 0.3$) and a Chabrier initial mass function (IMF).

2. Observations and data analysis

We observed the three brightest ALPINE objects (for a full discussion of the selection, see Devereaux et al. 2023) in [CII] (DEIMOS_COSMOS_818760, DEIMOS_COSMOS_873756, vuds_cosmos_5101218326),[1] using the C43-3 (~0.4″, 73 min) and C43-5 (~0.2″, 189 min) configurations (2019.1.00226.S). This is only a small fraction (17%) of the 30 h initially planned to study the dynamics, but it is sufficient for the goal of this Letter. In addition, we observed a massive and bright ALPINE rotator candidate VC5110377875 (2022.1.01118.S) in C43-4 (~0.3″) configuration during 286 min. These observations were supposed to be followed by higher-resolution observations (C43-7, ~0.07″), which were not completed.

The data were calibrated by the standard observatory pipeline, and imaged using the common astronomy software applications for radio astronomy (CASA; CASA Team et al. 2022). We produced continuum maps after excluding the [CII]-contaminated channels and the [CII] moment-0 maps (i.e., velocity-integrated line flux maps) after subtracting the continuum in Fourier space. For DC818760, DC873756, and VC5101218326 we also included the compact-configuration visibilities from the initial ALPINE observations to recover the large-scale components. This was not necessary for VC5110377875 since the full ALPINE integrated flux is already recovered by the new high-resolution observations alone. The data reduction is described in detail in a companion paper focusing on the morpho-kinematical analysis of these objects (Devereaux et al. 2023). The source properties and the achieved ALMA performance are listed in Table 1.

The [CII] flux is then used to derive the gas mass, while the rest-frame far-infrared continuum provides the dust obscured SFR. While initially considered to be an SFR tracer (e.g., De Looze et al. 2014; Capak et al. 2015), recent theoretical and observational studies pointed out that [CII] is more tightly connected to the molecular gas mass (e.g., Zanella et al. 2018; Madden et al. 2020; Vizgan et al. 2022; D'Eugenio et al. 2023; Ramambason et al. 2023), and correlates with SFR through the KS relation (e.g., Ferrara et al. 2019). The [CII] line also comes from the neutral and ionized medium, but their contribution is expected to be small in massive high-redshift galaxies (e.g., Vizgan et al. 2022). In addition, starbursting systems with short depletion timescales ($M_{\rm gas}/{\rm SFR} \sim 100\,{\rm Myr}$) tend to have low [CII]-to-IR luminosity ratios (Díaz-Santos et al. 2013; Gullberg et al. 2015), which should not be the case for an SFR tracer. A theoretical discussion about this [CII] deficit in starbursts can be found in Vallini et al. (2021). Finally, integrated [CII]-based gas masses of the ALPINE sample agree with dust-based measurements and dynamical estimates after subtracting the stellar masses (Dessauges-Zavadsky et al. 2020). A systematic comparison of the various tracers (CO, [CI], [CII], and dust) in high-z lensed dusty star-forming galaxies, with higher SFRs than our targets by a factor of 2–50, also found a good agreement between them (Gururajan et al. 2023). Contrary to CO, the [CII] line luminosity has a weak dependence on metallicity and is sensitive to CO-dark gas as shown by studies in nearby low-metallicity dwarfs (Madden et al. 2020; Ramambason et al. 2023).

The gas surface density ($\Sigma_{\rm gas}$) is derived from the [CII] moment-0 map $m_{\rm [CII]}$ in Jy km s^{-1} beam^{-1} using

$$\Sigma_{\rm gas} = \alpha_{\rm [CII]} \frac{1}{D_{\rm A}^2 \Omega_{\rm beam}} \left(1.04 \times 10^{-3} \frac{L_\odot\, s}{{\rm GHz\,Mpc^2\,Jy\,km}}\right) D_{\rm L}^2 \nu_{\rm obs} m_{\rm [CII]}, \quad (1)$$

where $\alpha_{\rm [CII]}$ is the [CII]-to-gas conversion factor (31 $M_\odot/L_\odot$, Zanella et al. 2018). This conversion factor has been cross-calibrated using CO up to $z \sim 2$ to measure the molecular gas mass. If the small expected fractional contribution from other phases to the [CII] luminosity in their sample and in our objects are similar, we should thus obtain directly a molecular gas mass corrected from the contribution of the rest of the interstellar medium. The parameter $D_{\rm A}$ is the angular diameter distance and $\Omega_{\rm beam}$ the solid angle of the synthesized beam defined as the integral of a beam after normalizing its peak to unity, $D_{\rm A}^2 \Omega_{\rm beam}$ being the physical area associated with the synthesized beam. The following factors in Eq. (1) correspond to the conversion from line flux to luminosity (Solomon et al. 1992) with $D_{\rm L}$ being the luminosity distance and $\nu_{\rm obs}$ the observed frequency.

The SFR surface density ($\Sigma_{\rm SFR}$) is the second quantity involved in the KS relation. In galaxies with a non-negligible dust content as ALPINE galaxies (Fudamoto et al. 2020), we can estimate the total SFR by combining the obscured SFR probed by the far-infrared ($\rm SFR_{IR}$) and unobscured SFR seen in the UV ($\rm SFR_{UV}$). The total SFR is the sum of these two values, and can be derived using (Madau & Dickinson 2014)

$${\rm SFR} = {\rm SFR_{UV}} + {\rm SFR_{IR}} = \kappa_{\rm UV} L_{\rm UV} + \kappa_{\rm IR} L_{\rm IR}, \quad (2)$$

where $L_{\rm UV}$ is the rest-frame 1500 Å luminosity and $L_{\rm IR}$ the total 8–1000 μm IR luminosity; $\kappa_{\rm UV}$ and $\kappa_{\rm IR}$ are the conversion factors with a value of $1.02 \times 10^{-10}\, M_\odot/L_\odot$ and $1.47 \times 10^{-10}\, M_\odot/L_\odot$ after converting to the Chabrier IMF.

The 158 µm rest-frame continuum map (m_{158}) in Jy/beam is converted into obscured SFR surface density ($\Sigma_{\rm SFR_{IR}}$) using

$$\Sigma_{\rm SFR_{IR}} = \kappa_{\rm IR} \frac{1}{D_A^2 \Omega_{\rm beam}} \frac{L_{\rm IR}}{L_{158}} \nu_{\rm cont} \frac{4\pi D_{\rm L}^2}{1+z} m_{158}, \quad (3)$$

where $\nu_{\rm cont}$ is the rest-frame continuum frequency, and $\frac{L_{\rm IR}}{L_{158}}$ is the ratio of the total luminosity to the 158 µm rest-frame

[1] Hereafter, we refer to DEIMOS_COSMOS_ as DC and vuds_cosmos_ as VC.

Table 1. Summary of the observations and achieved performance.

Source	RA h:min:s	Dec deg:min:s	$z_{[CII]}$	Beam size arcsec^2	σ_{cont} μJy/beam	$\sigma_{[CII]}$ Jy km s^{-1} beam^{-1}	5σ Σ_{gas} limit $M_\odot$/pc^2
DC818760	10:01:54.86	+2:32:31.54	4.5613	0.30×0.23	31	0.068	2000
DC873756	10:00:02.71	+2:37:40.20	4.5457	0.31×0.25	26	0.077	1940
VC5101218326	10:01:12.50	+2:18:52.72	4.5739	0.29×0.23	31	0.074	1920
VC5110377875	10:01:32.33	+2:24:30.41	4.5505	0.40×0.35	17	0.037	420

Notes. The σ_{cont} and $\sigma_{[CII]}$ column are the noise of the continuum map and the [CII] moment-0 map, respectively. The 5σ Σ_{gas} limit is derived from the gas surface density map obtained after applying the conversion from Eq. (1).

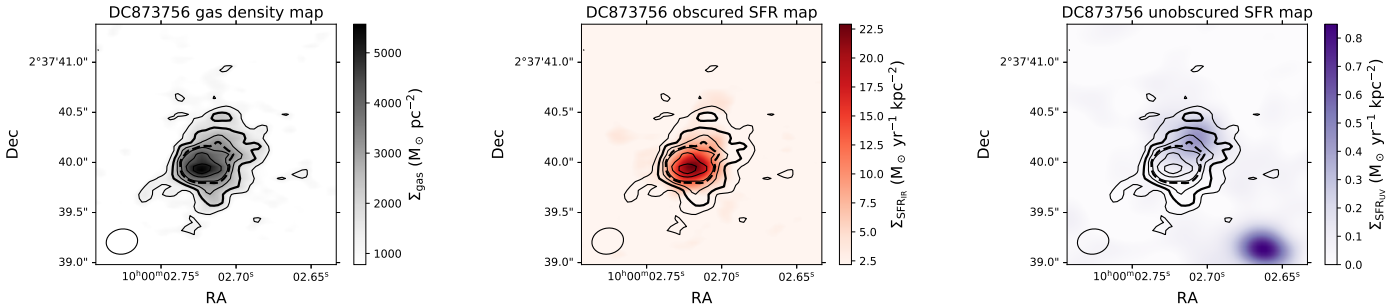

Fig. 1. Surface density maps of DC873756: Gas (left, traced by [CII]), obscured FIR SFR (center, traced by the 158 µm rest-frame continuum), and unobscured UV SFR (right, traced by the *F*814*W* observer-frame continuum). The black contours are the (3+2k)σ levels ($k \geq 0$) of the gas surface density. The thicker solid and dashed lines, respectively, are used to highlight the 5σ Σ_{gas} limit and the border between the low- and high-density regions used in our analysis (see Sect. 3). The ALMA synthesized beam size is shown in the lower left corner. The unobscured SFR surface density map based on HST data is convolved by a Gaussian kernel to match the ALMA resolution.

monochromatic luminosity. We use the value of 1/0.113 computed by Béthermin et al. (2020) based on *Herschel* stacking. This constant conversion factor assumes implicitly a constant dust temperature in our objects, and variations could lead to systematic effects on $\Sigma_{SFR_{IR}}$ estimates (Cochrane et al. 2022). Unfortunately, high-resolution observations at higher frequency to constrain the dust temperature in each line of sight are still out of reach even with ALMA.

To produce UV rest-frame maps, we started from cutouts of the HST COSMOS mosaics (Koekemoer et al. 2007) in the *F*814*W* filter (∼1480 Å rest-frame), and converted the instrumental units into physical units ($M_\odot$ yr^{-1} kpc^{-2}) using κ_{UV}, the luminosity distance, and the physical area at $z \sim 4.5$ corresponding to the HST pixel. To match the ALMA resolution, we then convolved the HST map by an elliptical Gaussian kernel with a major-axis width $\sigma^{ker}_{maj} = \sqrt{(\sigma^{ALMA}_{maj})^2 - \sigma^2_{HST}}$ (same formula for the minor axis), while ensuring that the normalization preserves the surface density. We tested this procedure on the HST PSF and found that the recovered beam is similar to the ALMA beam with an accuracy better than 10 %.

In Fig. 1 we present the surface density maps of DC873756 as an example, while the other sources are shown and briefly discussed in Appendix A. We note that the gas map has a very high S/N, and only the galaxy core is detected in the obscured SFR map. We also note that the obscured and unobscured SFR surface density maps exhibit different morphologies with the UV star formation coming mainly from the diffuse gas extension in the northwest and not the IR-bright core. The southwest bright UV blob has a robust photo-z of 3.4±0.1 (Weaver et al. 2022), and is thus probably not related to our target. This highlights the necessity to have access to both the obscured and unobscured star formation in our analysis. This source is thus asymmetric with a dusty star-forming core slightly offset in the southeast direction and a diffuse and less obscured extension in the northwest, illustrating the complexity of the morphologies at this redshift (see Devereaux et al. 2023 for more details).

3. Results

We first investigated the KS relation on a pixel-per-pixel basis (0.06″in VC5110377875 and 0.04″in the other galaxies). Since our Σ_{gas} map is by far the deepest, we restricted our study to the regions were the gas is detected in [CII] at better than 5σ (see Table 1) to robustly avoid working on noise spikes in the source outskirts. We then summed the $\Sigma_{SFR_{IR}}$ and $\Sigma_{SFR_{UV}}$ maps to obtain the Σ_{SFR} maps, and assumed a quadratic combination of the noise. In our objects, the obscured SFR contributes 75–99% of the total SFR. In Fig. 2 we show our results for each source. While in DC873756 most of the lines of sight have a Σ_{SFR} signal above 3σ, this is not the case in the three other sources. The risk of bias is very high in the Σ_{gas} regime where a small fraction of pixels are detected in Σ_{SFR}. In addition, in interferometry, the data points from the neighboring pixels are not independent because the noise is correlated at the scale of the synthesized beam. In this Letter we thus only focus on deriving unbiased average quantities, which unfortunately prevents us from studying the scatter.

For each source, we defined two different regions based on their Σ_{gas}. We cut the range between the 5σ limit and the maximum in two bins of the same logarithmic size, building two different regions with a lower and a higher Σ_{gas}. The high-density region tends to be in the center, while the lower-density region forms a ring around it (see Fig. 1). However, the disturbed morphologies of our systems lead to rather complex shapes, which justifies a posteriori not using radial profiles in this object type. Finally, we computed the mean Σ_{gas} and Σ_{SFR} in each region of each object. In Appendix C we describe a simulation validating

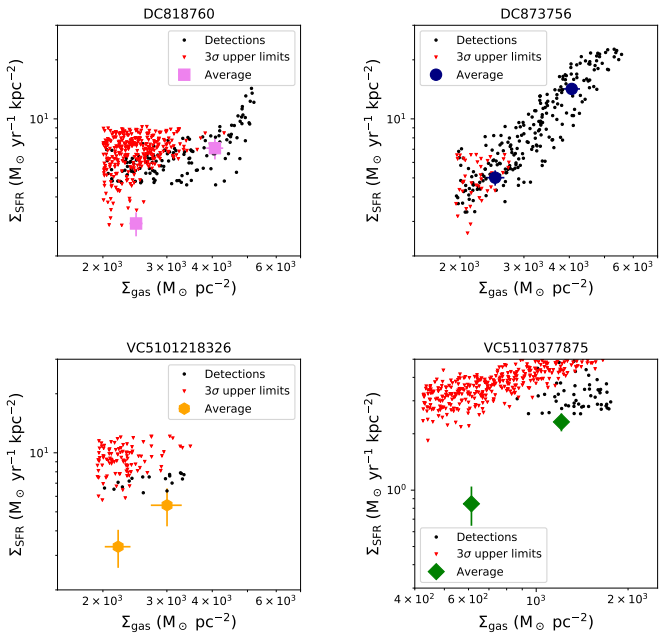

Fig. 2. Pixel-by-pixel KS relation between the SFR and gas surface density. Each panel corresponds to a source (upper left: DC818760, upper right: DC873756, lower left: VC5101218326, lower right: VC5110377875). The small black filled circles correspond to lines of sight with a $>3\sigma$ signal on the SFR surface density, and the small red downward triangles to 3σ upper limits. The large filled symbols (same as in Fig. 3) correspond to the average value for all the pixels in a given gas surface density bin (see Sect. 3 and Table 2).

our method. This simulation shows that we can recover without bias the intrinsic relation in the presence of noise. However, this simulation does not include the potential complex systematic effects from spatial variations of the conversion factors used in Eqs. (1)–(3).

To derive uncertainties on these quantities, we moved randomly the two regions in a noisy area of the map using the same offset for both regions, and measured our observables using the same method as previously. This process was repeated 10 000 times, and the standard deviation of the results provides the uncertainty. The results are summarized in Table 2. We also computed the typical correlation between the noise realizations in the two regions and found a Pearson correlation coefficient of 0.5 ± 0.1. This is expected since the two regions have a common border, and the interferometric noise is correlated at the scale of the synthesized beam. In Fig. 2 these average values are located at the middle of the cloud of points when most of the pixels are detected (DC873756 and high-density bin of DC818760), but lie significantly below otherwise. This is not surprising since in the regime of low average S/N the detections are biased toward positive outliers of the KS relation and the instrumental noise.

In Fig. 3 we present a synthesis of our results together with a compilation of previous works. All our data points but one are consistent with a 0.5–1 Gyr depletion timescale expected for massive main-sequence galaxies at $z \sim 4.5$ (Scoville et al. 2017; Dessauges-Zavadsky et al. 2020). The only outlier (285 ± 20 Myr) is the central high-density region of DC873756, which has the highest obscured SFR fraction ($\mathrm{SFR_{IR}/SFR_{tot}} = 98.7 \pm 0.3\%$) of the sample, and could thus hide a mild but heavily obscured starburst.

We compared our results with CO measurements of the global KS relation from the nearby COLD GASS sample

Table 2. Average gas ($\langle\Sigma_{\rm gas}\rangle$) and SFR ($\langle\Sigma_{\rm SFR}\rangle$) surface density measured in two $\Sigma_{\rm gas}$ bins for our four objects.

Name	$\Sigma_{\rm gas}$ range $M_\odot/\mathrm{pc}^2$	$\langle\Sigma_{\rm gas}\rangle$ $M_\odot/\mathrm{pc}^2$	$\langle\Sigma_{\rm SFR}\rangle$ $M_\odot\,\mathrm{yr}^{-1}\,\mathrm{kpc}^{-2}$
DC818760	2005–3232	2468±101	2.9±0.4
DC818760	3232–5208	4068±219	7.1±0.9
DC873756	1945–3291	2500±151	5.0±0.4
DC873756	3291–5570	4062±215	14.2±0.6
VC5101218326	1926–2590	2203±182	3.3±0.7
VC5101218326	2590–3481	3003±295	5.4±1.2
VC5110377875	424–862	613±37	0.8±0.2
VC5110377875	862–1755	1210±50	2.3±0.3

Notes. The uncertainties are derived using the Monte Carlo simulations described in Sect. 3. The uncertainties are based only on the instrumental noise.

(Saintonge et al. 2012) and the $z \lesssim 2.5$ PHIBBS and PHIBBS2 samples (Tacconi et al. 2013; Freundlich et al. 2019). We find that our objects are located in the scatter of these previous studies (~0.3 dex corresponding to a factor of 2), but with a higher gas surface density than most of the nearby sample by almost two orders of magnitude. Similarly, our sources are within a factor of 2 of the global KS relation fits by de los Reyes & Kennicutt (2019) at low redshift and by Wang et al. (2022) at high redshift, and the resolved low-z KS fit by Pessa et al. (2021). In contrast, most of the measurements of Nagy et al. (2023) at the scale of 1.6 kpc (compared to ~2 kpc in our analysis) in two strongly lensed $z \sim 1$ galaxies have significantly lower $\Sigma_{\rm SFR}$ at a given $\Sigma_{\rm gas}$ than other analyses; this is discussed in their paper without converging on a final explanation. Since their Cosmic Snake measurements agree with those of Pessa et al. (2021) and with our results, but not their measurements in the A521 galaxy, it could suggest that the A521 galaxy is an outlier. In contrast, our sample of main-sequence galaxies have significantly lower $\Sigma_{\rm SFR}$ at a given $\Sigma_{\rm gas}$ than typical high-redshift starbursts, which have an average depletion timescale of 100 Myr (Sharon et al. 2013; Rawle et al. 2014; Hodge et al. 2015). The $z \sim 7$ LBGs studied by Vallini et al. (2024) exhibit a similar behavior, suggesting that they could also be starbursting systems. Finally, we compared our results with the KS relation of Kraljic et al. (2023, fit for $z = 4$ and $10^8 < M_\star/M_\odot < 10^{9.5}$) from the hydrodynamical simulation NewHorizon (Dubois et al. 2021). Their results suggest a slightly higher normalization (by a factor of ~1.5) than our measurements. However, objects as massive as our targets are not found in the limited volume of their simulated box, and low- and high-mass high-z galaxies could exhibit different behaviors.

4. Discussion and conclusion

Our study suggests that main-sequence galaxies follow the same KS relation from $z = 0$ to $z = 4.5$, but exhibit a strong increase in their gas density with increasing redshift driving a rise in their SFR density. This universality of the KS relation for main-sequence galaxies might seem surprising considering how different local and $z > 4$ galaxies are, for example in term of gas fraction or sSFR. Since a significant fraction of our sample (Devereaux et al. 2023), and more globally of $z \sim 5$ massive main-sequence galaxies (e.g., Romano et al. 2021), are identified as possible mergers by morpho-kinematical analyses, this opens the question of a possible decoupling of the merging and starburst events in high-redshift galaxies, but also of the timescale

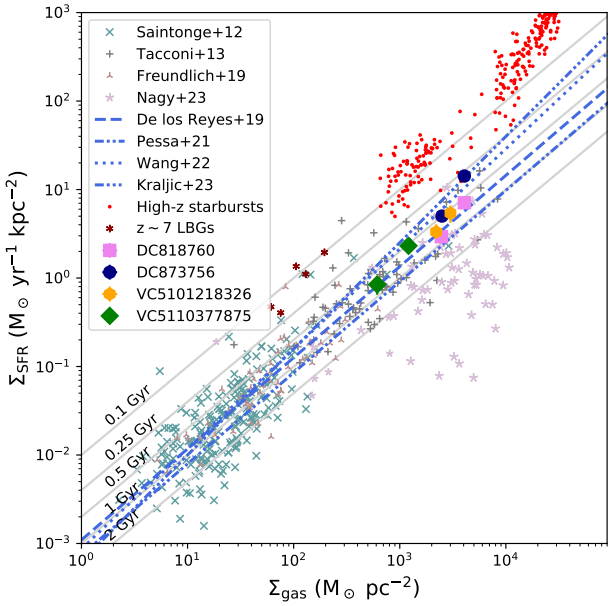

Fig. 3. Kennicutt-Schmidt relation between the SFR and gas surface density. The averaged data points from DC818760, DC873756, VC5101218326, and VC5110377875 are shown as violet squares, blue filled circles, yellow hexagons, and green diamonds, respectively. Our results are compared with the CO measurements of the global KS relation from the low-z COLD GASS sample (Saintonge et al. 2012, crosses) and at redshifts up to $z \sim 2.5$ from the PHIBBS (Tacconi et al. 2013, plus signs) and PHIBBS2 (Freundlich et al. 2019, three-branch stars) programs, together with the resolved KS relation in $z \sim 1$ lensed main-sequence galaxies (Nagy et al. 2023, five-branch stars). Also shown are the global (de los Reyes & Kennicutt 2019, dashed line) and resolved (Pessa et al. 2021, two-dot-dashed line) KS relations measured in the local Universe, the high-redshift global KS relation obtained by ALMA CO stacking (Wang et al. 2022, dotted line), and the global KS relation from simulations at $z \sim 4$ (Kraljic et al. 2023, three-dot-dashed line). The thin gray lines indicate the various depletion timescales. The red points are resolved measurements in high-z starbursts by Hodge et al. (2015). The brown six-branch stars are the measurements in $z \sim 7$ LBGs by Vallini et al. (2024). The error bars include only the uncertainties from the instrumental noise, but not from the calibration ($\sim$10 % for ALMA) or from the conversion factors used in Sect. 2. They are often smaller than the symbols.

of the SFR enhancement and the associated merger stage. Theoretical works suggest that high-z mergers could often be inefficient in increasing star formation (e.g., Fensch et al. 2017) because their turbulence-dominated medium is incapable of producing high-density regions, decreasing dramatically the gas depletion timescale (Segovia Otero et al. 2022). However, since extremely star-forming major starbursts are routinely observed in the submillimeter domain (e.g., Hodge & da Cunha 2020, for a review), we need to better understand the mechanism at play in the high-redshift Universe, and how they differ or not from low-z galaxies. Submillimeter galaxy selections could be either particularly efficient at finding the hypothetically rare and short starbursts at this epoch, or these more extreme objects may just have different physical conditions than our targets (e.g., different physical or dynamical properties of the pre-merger components). Objects, such as DC873756 that has a shorter depletion timescale in its obscured core, are particularly interesting for studying the intermediate regime.

Our analysis is a very first step. We need to confirm these results on larger samples and with other SFR (e.g., Hα with JWST) and gas tracers, since [CII] has not been tested at sub-galactic scale in the high-redshift Universe yet. Ideally, we should also push toward lower masses with potentially less mature systems and lower metallicities. Deeper ALMA observations would also allow us to detect the dust continuum in most lines of sight providing a local estimate of $\Sigma_{\mathrm{SFR_{IR}}}$, and measure the scatter on the KS relation. Finally, higher-resolution observations will test whether the KS relation breaks at smaller scales in main-sequence galaxies, as discussed in Nagy et al. (2023) at $z \sim 1$.

Acknowledgements. We thank Jackie Hodge for sharing her data compilation. This paper makes use of the following ALMA data: ADS/JAO. ALMA#2017.1.00428L, ADS/JAO.ALMA#2019.1.00226.S, ADS/JAO.ALMA #2022.1.01118.S. ALMA is a partnership of ESO (representing its member states), NSF (USA) and NINS (Japan), together with NRC (Canada), MOST and ASIAA (Taiwan), and KASI (Republic of Korea), in cooperation with the Republic of Chile. The Joint ALMA Observatory is operated by ESO, AUI/NRAO and NAOJ. This work was supported by the Programme National Cosmology et Galaxies (PNCG) of CNRS/INSU with INP and IN2P3, co-funded by CEA and CNES. E.I. acknowledges funding by ANID FONDECYT Regular 1221846. The Flatiron Institute is supported by the Simons Foundation. G.G. acknowledges support from the grants PRIN MIUR 2017 - 20173ML3WW_001, ASI n.I/023/12/0 and INAF-PRIN 1.05.01.85.08. Médéric Boquien gratefully acknowledges support from the ANID BASAL project FB210003 and from the FONDECYT regular grant 1211000. G.E.M. acknowledges the Villum Fonden research grant 13160 "Gas to stars, stars to dust: tracing star formation across cosmic time," grant 37440, "The Hidden Cosmos," and the Cosmic Dawn Center of Excellence funded by the Danish National Research Foundation under the grant No. 140. This work was supported by NAOJ ALMA Scientific Research Grant Code 2021-19A (HSBA). M.R. acknowledges support from the Narodowe Centrum Nauki (UMO-2020/38/E/ST9/00077) and support from the Foundation for Polish Science (FNP) under the program START 063.2023. Y.F. acknowledges support from JSPS KAKENHI Grant Number JP23K13149.

References

Béthermin, M., Daddi, E., Magdis, G., et al. 2015, A&A, 573, A113
Béthermin, M., Fudamoto, Y., Ginolfi, M., et al. 2020, A&A, 643, A2
Bigiel, F., Leroy, A., Walter, F., et al. 2008, AJ, 136, 2846
Capak, P. L., Carilli, C., Jones, G., et al. 2015, Nature, 522, 455
CASA Team, Bean, B., Bhatnagar, S., et al. 2022, PASP, 134, 114501
Cibinel, A., Daddi, E., Sargent, M. T., et al. 2019, MNRAS, 485, 5631
Cochrane, R. K., Hayward, C. C., & Anglés-Alcázar, D. 2022, ApJ, 939, L27
Daddi, E., Elbaz, D., Walter, F., et al. 2010, ApJ, 714, L118
De Looze, I., Cormier, D., Lebouteiller, V., et al. 2014, A&A, 568, A62
de los Reyes, M. A. C., & Kennicutt, R. C. 2019, ApJ, 872, 16
Dessauges-Zavadsky, M., Ginolfi, M., Pozzi, F., et al. 2020, A&A, 643, A5
D'Eugenio, C., Daddi, E., Liu, D., & Gobat, R. 2023, A&A, 678, L9
Devereaux, T., Cassata, P., Ibar, E., et al. 2023, A&A, submitted [arXiv:2311.11493]
Díaz-Santos, T., Armus, L., Charmandaris, V., et al. 2013, ApJ, 774, 68
Dubois, Y., Beckmann, R., Bournaud, F., et al. 2021, A&A, 651, A109
Elbaz, D., Daddi, E., Le Borgne, D., et al. 2007, A&A, 468, 33
Faisst, A. L., Schaerer, D., Lemaux, B. C., et al. 2020, ApJS, 247, 61
Fensch, J., Renaud, F., Bournaud, F., et al. 2017, MNRAS, 465, 1934
Ferrara, A., Vallini, L., Pallottini, A., et al. 2019, MNRAS, 489, 1
Freundlich, J., Combes, F., Tacconi, L. J., et al. 2013, A&A, 553, A130
Freundlich, J., Combes, F., Tacconi, L. J., et al. 2019, A&A, 622, A105
Fudamoto, Y., Oesch, P. A., Faisst, A., et al. 2020, A&A, 643, A4
Genzel, R., Tacconi, L. J., Gracia-Carpio, J., et al. 2010, MNRAS, 407, 2091
Gullberg, B., De Breuck, C., Vieira, J. D., et al. 2015, MNRAS, 449, 2883
Gururajan, G., B'ethermin, M., Sulzenauer, N., et al. 2023, A&A, 676, A89
Hodge, J. A., & da Cunha, E. 2020, R. Soc. Open Sci., 7, 200556
Hodge, J. A., Riechers, D., Decarli, R., et al. 2015, ApJ, 798, L18
Jones, G. C., Béthermin, M., Fudamoto, Y., et al. 2020, MNRAS, 491, L18
Jones, G. C., Vergani, D., Romano, M., et al. 2021, MNRAS, 507, 3540
Kennicutt, R. C., Jr. 1998, ApJ, 498, 541
Khusanova, Y., Bethermin, M., Le Fèvre, O., et al. 2021, A&A, 649, A152
Koekemoer, A. M., Aussel, H., Calzetti, D., et al. 2007, ApJS, 172, 196
Kraljic, K., Renaud, F., Dubois, Y., et al. 2023, A&A, submitted [arXiv:2309.06485]
Le Fèvre, O., Béthermin, M., Faisst, A., et al. 2020, A&A, 643, A1
Leroy, A. K., Walter, F., Sandstrom, K., et al. 2013, AJ, 146, 19
Madau, P., & Dickinson, M. 2014, ARA&A, 52, 415
Madden, S. C., Cormier, D., Hony, S., et al. 2020, A&A, 643, A141

Magdis, G. E., Daddi, E., Béthermin, M., et al. 2012, ApJ, 760, 6
Molina, J., Ibar, E., Smail, I., et al. 2019, MNRAS, 487, 4856
Nagy, D., Dessauges-Zavadsky, M., Messa, M., et al. 2023, A&A, 678, A183
Noeske, K. G., Weiner, B. J., Faber, S. M., et al. 2007, ApJ, 660, L43
Pessa, I., Schinnerer, E., Belfiore, F., et al. 2021, A&A, 650, A134
Ramambason, L., Lebouteiller, V., Madden, S. C., et al. 2023, A&A, in press, https://doi.org/10.1051/0004-6361/202347280
Rawle, T. D., Egami, E., Bussmann, R. S., et al. 2014, ApJ, 783, 59
Rodighiero, G., Daddi, E., Baronchelli, I., et al. 2011, ApJ, 739, L40
Romano, M., Cassata, P., Morselli, L., et al. 2021, A&A, 653, A111
Saintonge, A., Tacconi, L. J., Fabello, S., et al. 2012, ApJ, 758, 73
Saintonge, A., Lutz, D., Genzel, R., et al. 2013, ApJ, 778, 2
Sargent, M. T., Daddi, E., Béthermin, M., et al. 2014, ApJ, 793, 19
Schmidt, M. 1963, ApJ, 137, 758
Schreiber, C., Pannella, M., Elbaz, D., et al. 2015, A&A, 575, A74
Scoville, N., Lee, N., Vanden Bout, P., et al. 2017, ApJ, 837, 150
Segovia Otero, Á., Renaud, F., & Agertz, O. 2022, MNRAS, 516, 2272
Sharon, C. E., Baker, A. J., Harris, A. I., & Thomson, A. P. 2013, ApJ, 765, 6
Solomon, P. M., Downes, D., & Radford, S. J. E. 1992, ApJ, 387, L55
Sun, J., Leroy, A. K., Ostriker, E. C., et al. 2023, ApJ, 945, L19
Tacconi, L. J., Neri, R., Genzel, R., et al. 2013, ApJ, 768, 74
Vallini, L., Ferrara, A., Pallottini, A., Carniani, S., & Gallerani, S. 2021, MNRAS, 505, 5543
Vallini, L., Witstok, J., Sommovigo, L., et al. 2024, MNRAS, 527, 10
Vizgan, D., Greve, T. R., Olsen, K. P., et al. 2022, ApJ, 929, 92
Wang, T.-M., Magnelli, B., Schinnerer, E., et al. 2022, A&A, 660, A142
Weaver, J. R., Kauffmann, O. B., Ilbert, O., et al. 2022, ApJS, 258, 11
Zanella, A., Daddi, E., Magdis, G., et al. 2018, MNRAS, 481, 1976

[1] Université de Strasbourg, CNRS, Observatoire astronomique de Strasbourg, UMR 7550, 67000 Strasbourg, France
e-mail: matthieu.bethermin@astro.unistra.fr
[2] Aix Marseille Univ, CNRS, CNES, LAM, Marseille, France
[3] Department of Astronomy, University of Geneva, Chemin Pegasi 51, 1290 Versoix, Switzerland
[4] Instituto de Física y Astronomía, Universidad de Valparaíso, Avda. Gran Bretaña 1111, Valparaíso, Chile
[5] Dipartimento di Fisica e Astronomia, Università di Padova, Vicolo dell'Osservatorio 3, 35122 Padova, Italy
[6] INAF – Osservatorio Astronomico di Padova, Vicolo dell' Osservatorio 5, 35122 Padova, Italy
[7] IPAC, California Institute of Technology, 1200 E California Boulevard, Pasadena, CA 91125, USA
[8] Department of Physics, University of Oxford, Denys Wilkinson Building, Keble Road, Oxford OX1 3RH, UK
[9] Hiroshima Astrophysical Science Center, Hiroshima University, 1-3-1 Kagamiyama, Higashi-Hiroshima, Hiroshima 739-8526, Japan
[10] National Astronomical Observatory of Japan, 2-21-1, Osawa, Mitaka, Tokyo, Japan
[11] ARAID Foundation, Centro de Estudios de Física del Cosmos de Aragón (CEFCA), Unidad Asociada al CSIC, Plaza San Juan 1, 44001 Teruel, Spain
[12] Departamento de Astronomía, Universidad de La Serena, Av. Juan Cisternas 1200 Norte, La Serena 1720236, Chile
[13] Instituto de Alta Investigación, Universidad de Tarapacá, Casilla 7D, Arica, Chile
[14] Astronomy Department, University of Wisconsin, Madison, WI, USA
[15] Institut d'Astrophysique de Paris, CNRS and Sorbonne Université, UMR 7095, 98 bis Boulevard Arago, 75014 Paris, France
[16] Scuola Normale Superiore, Piazza dei Cavalieri 7, 50126 Pisa, Italy
[17] Astronomy Department, University of Massachusetts, Amherst, MA 01003, USA
[18] University of Bologna – Department of Physics and Astronomy "Augusto Righi" (DIFA), Via Gobetti 93/2, 40129 Bologna, Italy
[19] INAF – Osservatorio di Astrofisica e Scienza dello Spazio, Via Gobetti 93/3, 40129 Bologna, Italy
[20] Space Telescope Science Institute, Baltimore, MD 21218, USA
[21] Center for Computational Astrophysics, Flatiron Institute, 162 Fifth Avenue, New York, NY 10010, USA
[22] Department of Physics and Astronomy, University of California Davis, One Shields Avenue, Davis, CA 95616, USA
[23] Cosmic Dawn Center (DAWN), Jagtvej 128, 2200 Copenhagen N, Denmark
[24] DTU-Space, Technical University of Denmark, Elektrovej 327, 2800 Kgs. Lyngby, Denmark
[25] Niels Bohr Institute, University of Copenhagen, Jagtvej 128, 2200 Copenhagen N, Denmark
[26] Department of Space, Earth and Environment, Chalmers University of Technology, Onsala Space Observatory, 439 92 Onsala, Sweden
[27] Department of Astronomy, University of Florida, 211 Bryant Space Sciences Center, Gainesville, FL 32611, USA
[28] National Centre for Nuclear Research, ul. Pasteura 7, 02-093 Warsaw, Poland
[29] Center for Frontier Science, Chiba University, 1-33 Yayoi-cho, Inage-ku, Chiba 263-8522, Japan
[30] Dipartimento di Fisica e Astronomia, Universitá degli Studi di Firenze, Via G. Sansone 1, 50019 Sesto Fiorentino, Firenze, Italy
[31] INAF – Osservatorio Astrofisico di Arcetri, Largo E. Fermi 5, 50125 Firenze, Italy
[32] Center for Theoretical Astrophysics and Cosmology, Institute for Computational Science, University of Zurich, Winterthurerstrasse 190, Zurich, Switzerland
[33] Gemini Observatory, NSF's NOIRLab, 670 N. A'ohoku Place, Hilo, Hawai'i 96720, USA

Appendix A: Gas and SFR maps of the other sources

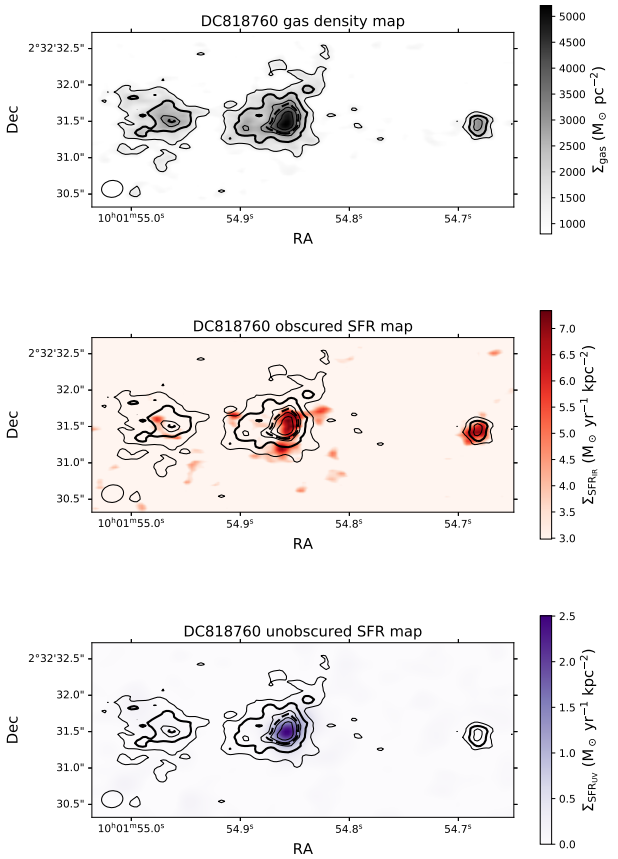

Fig. A.1. Same as Fig. 1, but for DC818760.

Figures A.1 and A.2 show the gas and SFR density maps of DC818760, VC5101218326, and VC5110377875, which are not discussed in the main text. Similarly to DC873756, we note that DC818760 and VC5101218326 have very different obscured and unobscured SFR density maps, confirming the need to have access to both. For instance, both the central and western components of DC818760 host an important obscured star formation activity, but only the central one is detected in the unobscured SFR density map. The morphology and the kinematics of these two objects is discussed in a companion paper (Devereaux et al. 2023; see also Jones et al. 2020 about the initial ALPINE data of DC818760). They are both identified as solid merger candidates. VC5110377875 will be studied in greater detail when the high-resolution data reaches a sufficient depth. So far it looks like a well-behaved rotator. However, we note a small displacement of the unobscured SFR toward the east compared to the gas.

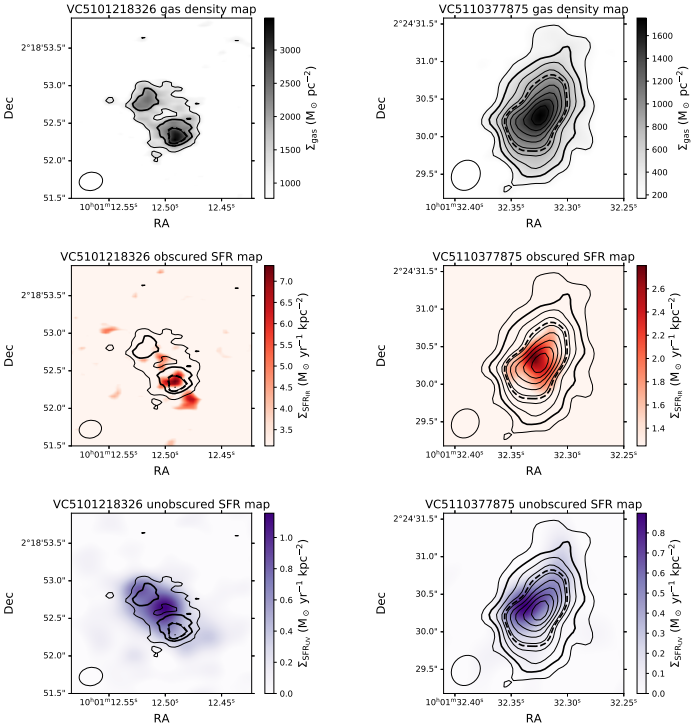

Fig. A.2. Same as Fig. 1, but for VC5101218326 (*left*) and VC5110377875 (*right*).

Appendix B: Depletion timescales measured inside apertures with various radii

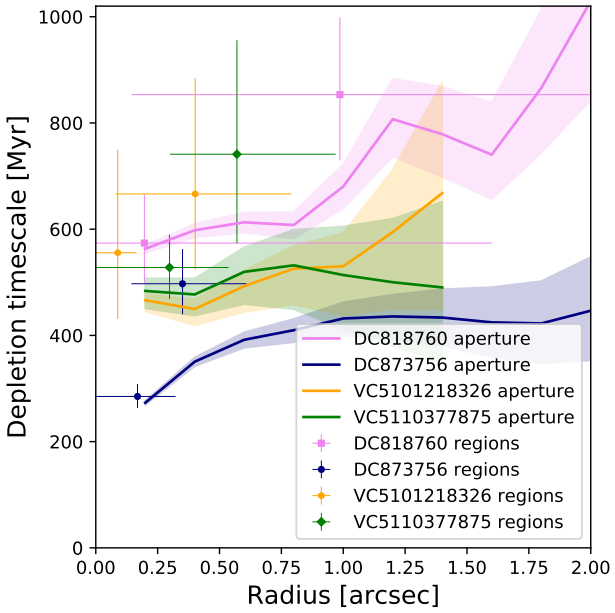

Fig. B.1. Gas depletion timescale measured in an aperture centered on the maximum of the [CII] emission as a function of its radius (solid lines, see Appendix B). The colored areas correspond to the 1σ uncertainties determined using the Monte Carlo sampling described in Sect. 3. For comparison, we represent the depletion timescales measured in our two Σ_{gas} regions using the same symbols as in Fig. 3. The horizontal error bars correspond to the full range of angular radial distances to the [CII] maximum in the region. The high-density region systematically corresponds to the smaller radius.

Since our targets have complex morphologies, we decided to measure the average Σ_{SFR} in regions selected to be in a specific range of Σ_{gas}. This type of measurement is easy to reproduce in simulations. This method is particularly well suited for z>4 observations since the [CII] line used as a gas tracer usually has a better S/N (by a factor of ∼3) than the dust continuum tracing the obscured SFR. It is not the case at lower redshift, where the gas tracers are often shallower than SFR estimators. Usually, the gas and SFR surface densities are measured in an aperture corresponding to the source size. This leads to multiple questions about the choice of wavelength or line to measure the source size, but also the exact definition of the source radius.

To compare the two approaches, we measured the gas depletion timescale in apertures centered on the maximum of the [CII] emission with various radii. This choice may appear arbitrary, but the UV center is often not representative of the mass distribution of the system because of the dust attenuation, and to date we have no access to high-resolution rest-frame near-infrared data probing the old stars. The uncertainties are determined using the same Monte Carlo resampling method that we used for the Σ_{gas} regions in Sect. 3. The comparison of the two approaches is shown in Fig. B.1 (solid lines). We note that two sources have a significantly longer gas depletion timescale for large aperture radii (DC818760, DC873756), while the two others do not exhibit any significant trend (VC5101218326, VC5110377875). DC818760 is a multi-component system and the large radii include the two neighbors, while the small radii only include the central component. It is not surprising to find slightly different timescales in the various components. As discussed in Sect. 3, DC873756 probably hosts an obscured starbursting core with a short depletion timescale, while it is longer in the outskirts.

In Fig. B.1 we also show the gas depletion timescales found in our low- and high-Σ_{gas} regions. The x-axis position of these datapoints corresponds to the average angular radial distance to the maximum of the [CII] emission. The error bars represent the full range of distances. Since the morphologies are not centro-symmetrical, there is an overlap between the two regions in terms of radial distance. The high-density regions correspond to smaller radii and agree with aperture measurements at the 1σ level. This is not the case of the low-density regions at larger radii for which the disagreement can reach $2\,\sigma$. However, the aperture measurements are cumulative and includes all the pixels from the center to the edge of the aperture. The two approaches are thus not measuring exactly the same thing, and a disagreement is expected if there are longer depletion timescales in the outskirts. However, the maximum disagreement caused by the choice of definition does not exceed 50 %, and is thus smaller than the scatter on the relations (typically a factor of 2). Consequently, the choice of the approach used to determine surface densities does not change the results qualitatively.

Appendix C: Testing the method measuring the mean gas and SFR surface densities

We built a simulation to test the accuracy of our method to derive mean Σ_{gas} and Σ_{SFR} (see Sect. 3). We produced cases based on DC873756 (hereafter case 1), for which most of the pixels in both the low and high gas density regions are detected in the combined Σ_{SFR} map, and VC5110377875 (case 2), for which most of the pixels in the low-density region are undetected. The first source is modeled by a symmetrical Gaussian with a FWHM of 0.5", and the second by a 1.5"×0.5" elliptical Gaussian. We convolved these models by the associated synthesized beams in the real observations and rescaled the peak of the convolved maps to match the observed values. We thus obtained three noiseless maps (Σ_{gas}, $\Sigma_{SFR_{IR}}$, $\Sigma_{SFR_{UV}}$) for each source. Since we applied a simple rescaling to our models, the local depletion timescale is thus constant across the simulated objects by construction. Finally, we added interferometric noise to the Σ_{gas} and $\Sigma_{SFR_{IR}}$ maps after rescaling it to the observed values, and white noise smoothed by our convolution kernel to the $\Sigma_{SFR_{UV}}$ map after matching its level to the observed value.

We then applied the same measurement process as described in Sect. 3 on both noiseless and noisy maps. The results are presented in Fig. C.1. The KS relation in the noiseless case is our reference (light blue small squares). Since there is no noise associated with these maps, we used the noise level of the Σ_{gas} noisy map to define the region above the 5σ density limit in which we analyzed individual pixels. The low and high gas density regions are defined in a similar way, and we derived the mean Σ_{gas} and Σ_{SFR} in each of them (dark blue large squares). As expected, there is a near perfect agreement between the individual pixels and the mean measurements in the two simulated objects.

We also analyzed the noisy maps. The various regions used in our analysis can slightly change compared to the noiseless case, since some pixels can pass above or below a threshold because of the noise. The individual detected pixels (small black filled circles) agree with the noiseless relation in case 1 where the S/N is high. In case 2 the detections agree only at the high-Σ_{gas} end, but are systematically higher than the noiseless case at the low-Σ_{gas} end. Since only pixels with Σ_{SFR} above $2.5\,M_{\odot}\,\mathrm{yr}^{-1}\,\mathrm{kpc}^{-2}$ are detected, only the positive noise outliers

are detected in the low-Σ_{gas} regime for which the average Σ_{SFR} is below this limit. In contrast, the mean values measured in the low and high gas density regions (dark green pentagons) agree at 1σ with the noiseless relation. To check for a possible bias, we computed their average positions over 1000 noise realizations (light green hexagons), and they agree at better than 3 % with the noiseless case.

Our simulation confirms that mean measurements over several well-selected regions are more effective at recovering mean Σ_{SFR} than individual pixel measurements, which are strongly biased in the low S/N regime. It is not surprising, since these regions encompass several synthesized beams and averaging them improves the S/N by approximately a factor of $\sqrt{N_{sb}}$, where N_{sb} is the number of synthesized beams in the region.[2] However, this method works only because we benefit from deep Σ_{gas} maps to select these regions.

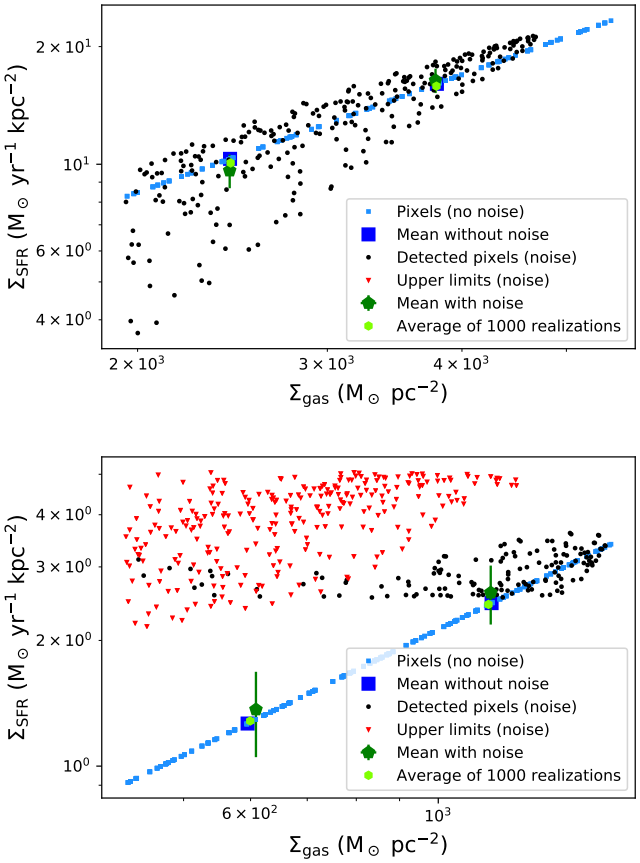

Fig. C.1. Kennicutt-Schmidt relation between the SFR and gas surface density in our simulation described in Appendix C. The panels correspond to two different simulated objects based on DC873756 (*upper panel*) and VC5110377875 (*lower panel*), illustrating different S/N regimes. The small blue squares show the pixels of the noiseless map, and the large dark blue squares are the mean computed in the low and high gas density regions (see Sect. 3). The small black filled circles are the 5σ SFR detections in the noisy maps, and the small red downward-facing triangles are the 3σ upper limits of non-detections. The dark green filled pentagons are the mean values measures in the two gas density regions. The small light green hexagons are the averages of these mean measurements over 1000 noise realizations.

[2] This is an approximation since the shape of the regions and the spatially correlated interferometric noise are both complex, but it works with a 20 % accuracy in our simulations.